Applied Surface Science 619 (2023) 156748

Contents lists available at ScienceDirect

Applied Surface Science

journal homepage: www.elsevier.com/locate/apsusc

Full Length Article

A novel two-step route to unidirectional growth of multilayer MoS_2 nanoribbons

Denys I. Miakota [a,*], Ganesh Ghimire [a], Rajesh Kumar Ulaganathan [a], Moises E. Rodriguez [b], Stela Canulescu [a,*]

[a] Department of Electrical and Photonics Engineering, Technical University of Denmark, Frederiksborgvej 399, Roskilde DK-4000, Denmark
[b] Department of Energy Conversion and Storage, Technical University of Denmark, Kgs. Lyngby DK-2820, Denmark

ARTICLE INFO

Keywords:
2D materials
TMDs
MoS_2
Chemical Vapor Deposition (CVD)
Pulsed Laser Deposition (PLD)
MoS_2 nanoribbons

ABSTRACT

Alkali-assisted chemical vapour deposition (CVD) of transition metal dichalcogenides (TMDs) has been shown to promote the growth of large single crystals of TMD monolayers. The morphology control of TMDs is a key parameter for the scalable synthesis of versatile layered materials. This work demonstrates that the alkali-assisted synthesis provides a route toward fabricating highly crystalline MoS_2 nanoribbons. Our proposed method involves a vapour-liquid–solid phase reaction between MoO_x **(2 < x < 3)** precursors grown by Pulsed Laser Deposition (PLD) and metal alkali halide (i.e., NaF). The growth process evolves via the emergence of the Na–Mo–O liquid phase, which mediates the formation of MoS_2 multilayer nanoribbons in a sulfur-rich environment. Moreover, the as-grown MoS_2 nanoribbons are surrounded by mono- and multilayer triangles of MoS_2 and exhibit a preferential alignment defined by both MoS_2 crystal symmetry and the underlying Al_2O_3 substrate. In addition, we observe a significant built-in strain in the as-grown MoS_2 nanostructures, which increase in magnitude from the multilayer nanoribbons to the triangular monolayers, and which can be effectively released upon transfer onto another substrate. The growth method developed here can enable flexibility in designing nanoelectronic devices based on TMDs with tunable dimensions.

1. Introduction

The growth of thin films is a fundamental basis for the modern semiconductor industry, which has already enabled the fabrication of many semiconductor devices with superior performance [1]. The advances in crystal growth and thin film fabrication opened new avenues for applied and fundamental research, as strong anisotropy can be introduced [2–4]. This also encourages a continuous search for novel materials for applications in optoelectronics, micro- and nanoelectronics [5]. In recent years, this has led to an exploration of low-dimensional materials, including (but not limited to) carbon nanotubes (CNT) [6,7], graphene [8–10], two-dimensional (2D) transition-metal dichalcogenides (TMDs) [11–13], nanoribbons (NRs) [14,15], and nanowires [16,17]. A key feature of these nanostructures is that their physical, chemical or mechanical properties significantly differ from their bulk counterparts.

The research for 2D materials, which emerged after the discovery of graphene, has evolved far beyond it. Layered TMD crystals of MoS_2, $MoSe_2$, WS_2, and WSe_2 are the most explored [18]. These materials can be thinned down to a single layer and possess an indirect-to-direct bandgap transition with a thickness reduction to a monolayer (ML). TMDs as bulk crystals and 2D layers exhibit a bandgap of 1–2 eV [19]. This makes the TMDs particularly interesting for light absorption and emission applications and drove a rapid development of the synthesis methods. A variety of methods have been explored, including chemical vapour deposition (CVD) [20–22] and metal–organic CVD (MOCVD), which provide superior-quality MLs. Other synthesis methods are liquid and ultrasonic exfoliation [23], physical vapour deposition [24], various two-step processes of pre-deposited precursor sulfurisation or selenization in a CVD furnace [25,26], molecular beam epitaxy [27,28], pulsed laser deposition (PLD) [29–31] or two-step processes based on PLD [32–34], atomic layer deposition [35–37].

The nanostructuring of TMDs into nanoribbons allows for efficient interaction between light and matter [38,39]. Controlling the geometrical dimensions of TMDs from 2D to 1D provides an additional degree of freedom in their electronic and optoelectronic properties. Moreover, the

* Corresponding authors.
E-mail addresses: denmi@fotonik.dtu.dk (D.I. Miakota), stec@fotonik.dtu.dk (S. Canulescu).

https://doi.org/10.1016/j.apsusc.2023.156748
Received 14 October 2022; Received in revised form 10 February 2023; Accepted 12 February 2023
Available online 15 February 2023

termination of the edges of MoS_2 nanoribbons leads to distinct electronic and magnetic properties. Zigzag MoS_2 nanoribbons show magnetic behaviour, while armchair MoS_2 nanoribbons are nonmagnetic [40]. In addition, theoretical calculations have shown that their properties can be tuned by strain [41]. CVD bottom-up synthesis efforts were devoted to the influence of metal-halide promoters [42] and substrate [43] on nanoribbon growth. Recent works have demonstrated the integration of TMD nanoribbons in photodetectors and field-effect transistors [44,45]. Hence, developing facile methods for the controlled growth of TMDs nanoribbons will encourage the integration of TMDs in optoelectronic devices.

In this study, we report on the alkali-induced directional growth of MoS_2 crystals on (0001) sapphire. The precursors are thin films of MoO_x ($2 < x < 3$) grown by PLD in the Ar background atmosphere, which enables the deposition of epitaxial oxides with an oxygen deficiency tunable in a broad range [34]. We reveal that solid oxide-to-sulfide conversion assisted by metal halide (NaF) promotes the directional growth of MoS_2 multilayer nanoribbons. The growth of aligned nanoribbons likely occurs in an alkali-assisted vapour-liquid–solid (VLS) phase reaction at elevated temperatures. We hypothesise that the MoS_2 nanoribbon bottom layer aids the growth of single-layer nanoribbons. A substantial oxygen deficiency in molybdenum oxide precursor may further enhance the growth of multilayer crystals in a preferential direction defined by 2H-MoS_2 crystal symmetry and the underlying substrate.

2. Materials and methods

2.1. Pulsed laser deposition of oxide precursors

The approach for the fabrication of the MoS_2 nanoribbons is shown in Fig. 1. In the first step, MoO_x precursors are deposited by PLD using a 248 nm KrF laser, as described in previous work [34], similarly to [32]. The MoO_x thin films were grown via laser ablation of a one-inch MoO_3 target (99.9% purity, from Testbourne Ltd.) in Ar at 1×10^{-1} mbar using a number of laser pulses varying between 10 and 40. The films were deposited on (0001) Al_2O_3 substrates of $1 \times 1\ cm^2$. In the second step, a thin NaF layer (20 nm thick) was deposited using thermal evaporation (Fig. 1b).

2.2. Sulfurization of MoO_x + NaF precursors

The sulfurisation step of the MoO_x precursors is shown in Fig. 1c. Firstly, the films were placed facing up on a flat ceramic plate and loaded

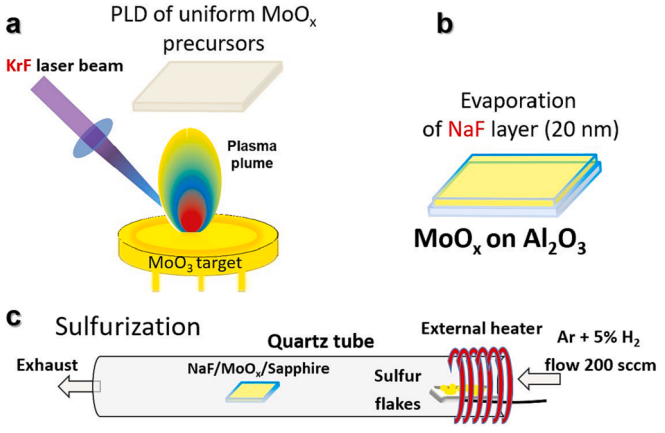

Fig. 1. The experimental setup for synthesising MoS_2 nanoribbons based on two-step processes involving Pulsed Laser Deposition (PLD). a) PLD of epitaxial MoO_x thin films at 700 °C. b) NaF (20 nm) layer deposition using thermal evaporation. c) Oxide to sulfide conversion in a sulfur-rich atmosphere at 900 °C.

in the middle of the three-zone tube furnace inside a quartz tube of 3 in. outside diameter. A narrow alumina ceramic boat containing 2.0 g of sulfur flakes (99.99% purity, from Sigma Aldrich) was placed outside the main heating area of the quartz tube and heated independently. Secondly, the system was pumped down to 5×10^{-3} mbar and sequentially flushed five times by pressuring to 400 mbar with Ar-H_2 gas mixture (5% volume fraction, 5.5 N purity) to remove residual gases, such as oxygen and water vapour. Then, a 200 sccm Ar-5% H_2 gas flow was introduced as a carrier gas throughout the process, making the base pressure 0.8 mbar. The tube furnace was then heated at a rate of 15 °C/min to 900 °C. When the furnace temperature was close to 900 °C, the external heater was set to 240 °C to produce an adequate sulfur evaporation rate. The sulfurisation process occurred at 900 °C for 15 min. The system was finally cooled down naturally to room temperature, with a furnace lid lifted at 400 °C. The estimated cooling rate from the growth temperature 900 °C to 650 °C was 20 °C/min, followed by a lower cooling rate of approximately 10 °C/min down to 400 °C when the furnace lid was open.

2.3. SEM measurements

The morphologies of the MoS_2 specimens were analysed using a Zeiss Merlin SEM equipped with an In Lens electron detector. The images were acquired at an acceleration voltage of 1.5 kV and a working distance between 3 and 4 cm.

2.4. AFM measurements

The AFM images were performed on a Bruker Icon AFM microscope, type AFM-Icon PT2. The measurements were performed in a tapping mode in the air using AFM probe type Tap150AI-G (from BudgetSensors).

2.5. Raman and PL spectroscopy

Raman spectra were collected using a home-built confocal Raman spectroscopy setup with a 532 nm excitation laser. The spectrometer is a Spectra Pro HRS750 scanning monochromator from Princeton Instruments equipped with three gratings of 300 *gr/mm*, 1200 *gr/mm*, and 1800 *gr/mm* and a cryogenically-cooled, and an ultra-low noise Pylon CCD camera, type PyLoN:100BR. The wavelength calibration was carried out using an Ar-Ne light source mounted to the entrance slit of the spectrometer. The spectrometer resolution was found to be 0.4 cm^{-1}. Raman spectra were collected using various integration times and then normalised. The spectra were acquired using a power below 10 mW to prevent samples from overheating. Raman mapping was performed on a Renishaw inVia Reflex confocal Raman spectrometer and using a 2400 *gr/mm* grating with adjusted integration time, a 532 nm excitation laser with 5 mW power, and maps with a step size of 300 nm. The spectra were calibrated using the Si Raman peak at 520.5 cm^{-1}.

2.6. XPS spectroscopy

X-ray photoelectron spectroscopy (XPS) was performed using Thermo Fisher Nexsa XPS system with Al K_α 1486.6 eV excitation source, and a flood gun was used for charge compensation. The energy scale of the XPS was calibrated using $Au4f_{7/2}$ line centred at 84.0 eV, and XPS line positions were adjusted using the C1s peak of the surface carbon at 284.6 eV, which is present in all the samples.

3. Results and discussion

The morphology of the MoS_2 nanoribbons. Fig. 2 shows the optical (a) and SEM (b) images of the MoS_2 nanoribbons obtained upon sulfurisation of the NaF/MoO_x layer stack. The MoO_x film was deposited using 30 laser pulses. The chemical composition of the MoO_x films was

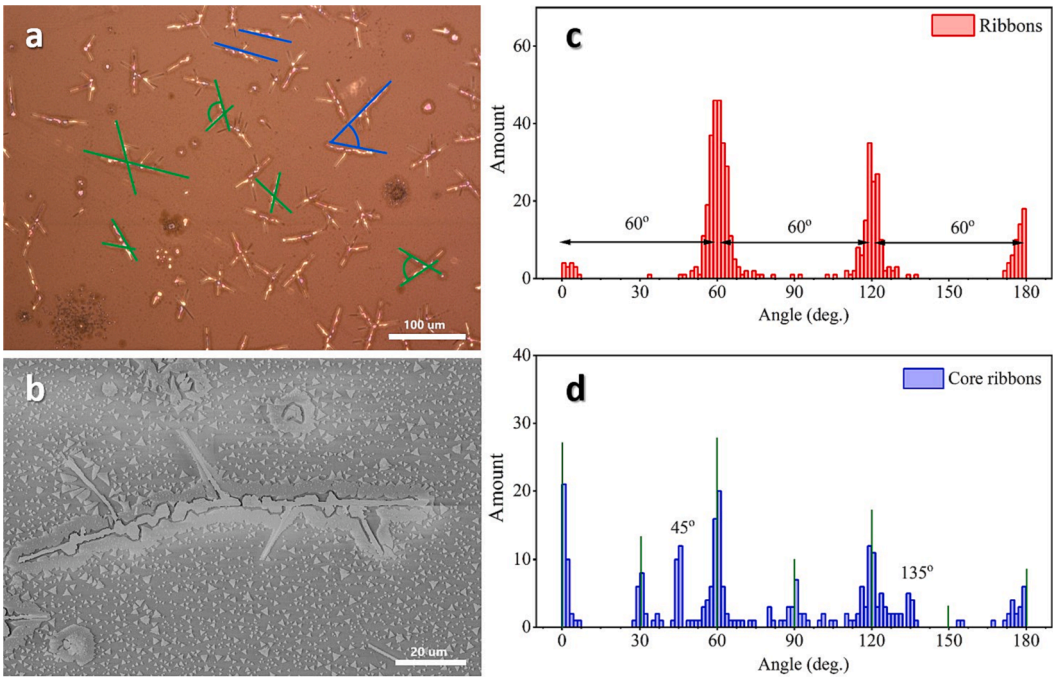

Fig. 2. The morphology of the MoS_2 nanoribbons obtained upon sulfurization of the NaF/MoO_x stack. a) Optical image of the MoS_2 nanoribbons, bright field. The green and blue lines indicate the ribbons' growth directions. b) In Lens SEM image of a single MoS_2 tree-like structure with smaller nanoribbons as branches. c) The angular distribution of the MoS_2 nanoribbons with respect to their nearest neighbors. d) The angular distribution of the MoS_2 core nanoribbons' directions with respect to their neighbours.

analysed by XPS, as shown in Fig. S1, S2, and S3. In contrast to the conventional CVD process, the precursor films grown by PLD have reduced molybdenum oxide with a high fraction of Mo^{6+} (>57.5%), followed by smaller contributions from Mo^{5+} and Mo^{4+}. The coloured lines in Fig. 2 indicate the growth directions of the nanoribbons on the sapphire. Fig. 2c shows the angular distribution of the nanoribbons with respect to their nearest neighbours, extracted from the optical image in Fig. 2a and additional optical images shown in Figs. S4 and S5. Both optical and SEM images reveal the presence of tree-like structures consisting of merged nanoribbons with a visible core. It is worth noting that the side branches expanding from the core exhibit well-defined alignment, which can be seen in Fig. 2c. The nanoribbons have a preferential orientation of 0°, 60°, 120° or 180° with respect to their nearest neighbours (as indicated by the green lines in Fig. 2a), which points at a 6-fold symmetry. This is the case for both MoS_2 and the hexagonal sapphire substrate. A 60° angle between the growth directions suggests that MoS_2 crystal facets guide the growth of the nanoribbons from the core.

Moreover, we have extracted the angle between separated core ribbons of the tree-like structures (indicated by the blue lines in Fig. 2a), which is shown as a histogram in Fig. 2d (green markers are for eyes guidance). The pronounced peaks at 0°, 30°, 45°, 60°, 90°, 120° or 180° give a peak separation of either 30° or 30°/2. This points at the core ribbons' preferred orientation and corresponds to a 6-fold symmetry. Hence, this strongly indicates that the underlying sapphire substrate guides the growth of the MoS_2 crystals since

the different nanoribbons grow independently. Epitaxial growth is energetically favourable between the MoS_2 crystal and hexagonal Al_2O_3 (0001) plane. Dedicated calculations on the strain-dependent alignment of the 2H-MoS_2 and alpha-Al_2O_3 supercells reported by Dumcenco et al. [46]. The built-in strain in 2D MoS_2 ranges from 0.1% for 0° angle to 3.8% for an angle of θ of 30°. As discussed later, the growth initiates from MoS_2 seed crystals, and the facets of these crystals serve as nucleation sites for the crystallisation and unidirectional expansion of the nanoribbons.

Next, we investigate the morphology of the MoS_2 nanoribbons and their formation mechanism. High-resolution SEM images of the MoS_2 nanoribbons are shown in Fig. 3 (see also Fig. S6 and S7 in the SI). Here we used the InLens detector for SEM imaging, providing higher spatial resolution than the high-energy secondary electron detector. The uniformity in thickness of the MoS_2 nanoribbons across their widths and lengths can be inferred from the uniform colour contrast of the SEM images. Moreover, Fig. 3 shows that nanoribbons are typically surrounded by monolayers of MoS_2, which may originate from the nanoribbons' edges. A magnified view of the MoS_2 nanoribbon's edge in Fig. 3c reveals that MoS_2 grows in directions defined by the hexagonal MoS_2 crystal symmetry.

The edges of the MoS_2 specimens shown in Fig. 3b,c exhibit saw-like profiles, with triangular "teeth" parallel to each other and the vertex close to the ideal angle of 60°. These layers are likely to emerge after the nanoribbon formation. The bottom layer of the MoS_2 nanoribbon (the layered structure of a nanoribbon can be seen in Fig. S8a,c) serves as a nucleation site for the MoS_2 domain growth originating upon exposure of residual Mo-containing liquid phase to sulfur vapour. Hence, the MoS_2 nanoribbon facilitates the lateral expansion of the single-layer nanoribbon MoS_2 domains. Moreover, the SEM images in Fig. 3d,e reveal the presence of bulk crystals without a preferential orientation, likely originating from large liquid droplets. Lastly, the MoS_2 nanoribbons exhibit local ruptures, as shown in Fig. 3f.

Fig. 4 shows the AFM images of individual MoS_2 nanoribbons. The scanning area of $10 \times 10\ \mu m^2$ is insufficient to capture a nanoribbon. The uniform and long MoS_2 nanoribbons have a sharp 60° termination angle (see also SEM in Fig. S7b, and AFM in Fig. S9). In strong contrast to SEM, AFM has a poor depth of field, i.e., instrument capability to resolve features with large height differences. Hence, the sharp thickness difference between the bulk nanoribbon and adjacent monolayer makes the monolayer edge not visible in the AFM images. The well-defined angle at the edge suggests that the nanoribbon growth direction is determined by 2H-MoS_2 crystal symmetry. The AFM line profiles of the nanoribbons in the lower panels in Fig. 4 show a rectangular-like profile with a sharp slope along the nanoribbon's edges with a flat top visible both in AFM and SEM Fig. S7. This also can be identified in Fig. S8b. The thickness of

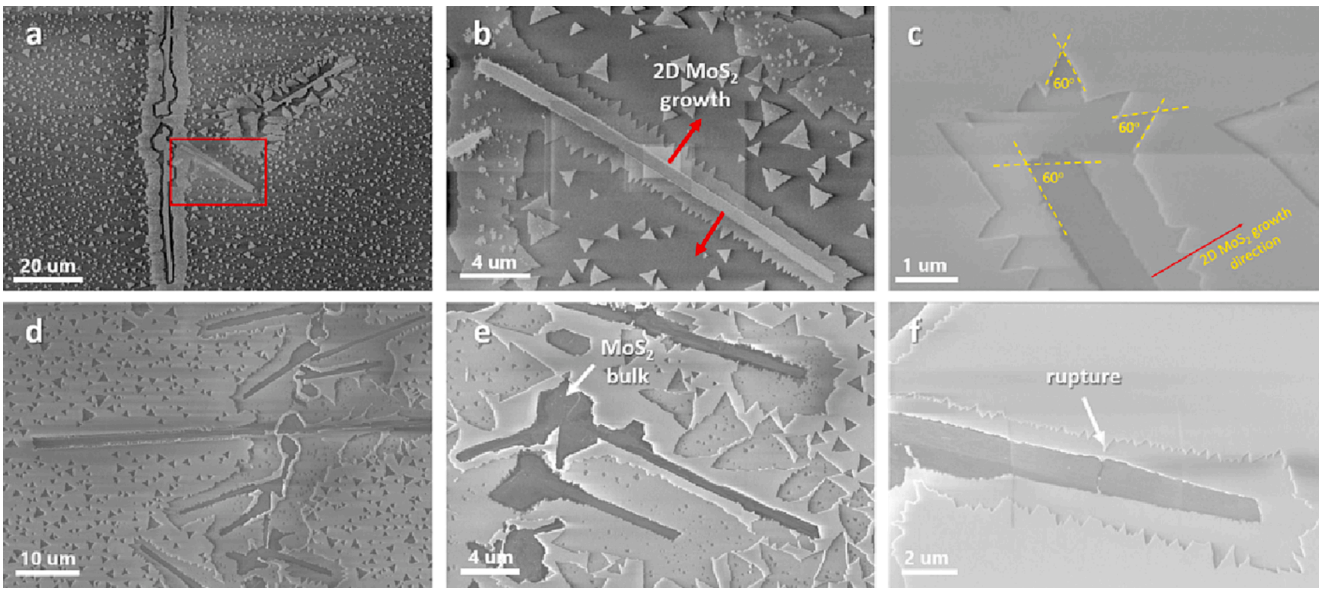

Fig. 3. SEM images of MoS_2 nanoribbons. a) SEM image of a large MoS_2 nanoribbon. The red frame highlights a smaller nanoribbon expanding from it. b) High magnification SEM image of the MoS_2 nanoribbon in the red frame in (a). The 2D MoS_2 triangular crystals surround the nanoribbon. c) SEM image of a MoS_2 nanoribbon edge. d) MoS_2 nanoribbons together with a thick crystal presence. e) High magnification SEM image of MoS_2 nanoribbons present together with MoS_2 single layer and bulk crystal. f) Fracture of a multilayer MoS_2 nanoribbon. The monolayer nanoribbon around the multilayer parent is evident.

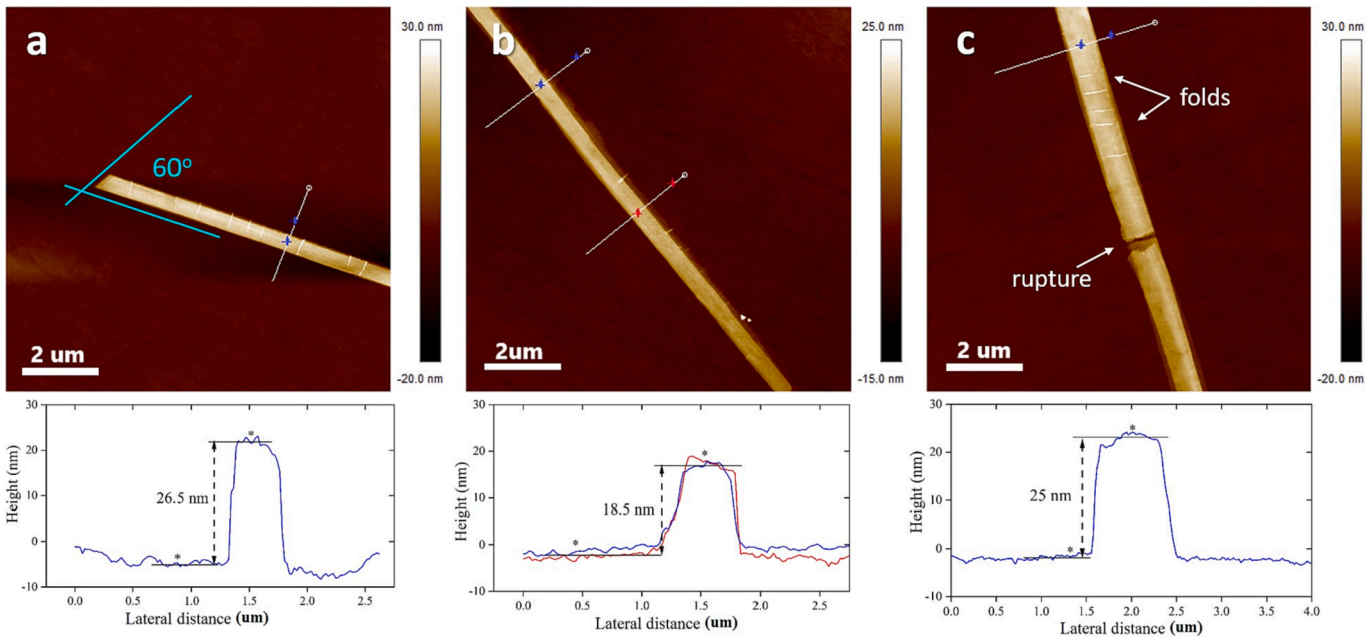

Fig. 4. AFM images of MoS_2 nanoribbons. a) MoS_2 nanoribbon and its edge featuring a 60° angle. b) The middle part of MoS_2 nanoribbon. c) Folds and crystal rupture in the MoS_2 nanoribbon. The corresponding line profiles of the nanoribbon reveal a layered structure.

MoS_2 nanoribbons ranges between 18.5 ± 0.05 and 25.5 ± 0.05 nm (see Fig. S10 in the SI), their widths are typically around 800 ± 200 nm, and the length-to-width ratios vary from 20 to 30, which denotes multilayer MoS_2 nanoribbons. The AFM line profile in Fig. 4b shows that nanoribbons exhibit a uniform thickness profile across their length, with occasional MoS_2 layer steps. The average values of thickness and width for different nanoribbons are presented in Fig. S10 in the SI. In addition, the AFM images reveal two distinct cases of structural defects during the growth, i.e., nanoribbon folds (Fig. 4a,b) and ruptures (Fig. 4c). These microfaults may occur during rapid cooling from 900 °C after sulfurisation. Folded parts of the top layers likely appear due tcrystal's rupture, which relaxes the strain of the top MoS_2 layers. The growth of a nanoribbon with uniform thickness and width suggests its formation from a liquid phase by directional propagation of a crystal. Additionally, as shown in Fig. 3, the nanoribbons are typically surrounded by 2D MoS_2 crystals which can also be identified in Fig. S11. We extracted the thickness of these crystals using an area-averaged line profile, which gives us an average thickness of 0.80 ± 0.10 nm. This value corresponds to a single MoS_2 layer and is valid for most of the triangular crystals observed.

The growth mechanism of the MoS_2 ribbons. The unidirectional growth of the nanoribbons indicates a restructuring of the uniform precursor at high temperatures, which occurs via a transition through a liquid phase and subsequent crystallisation. The alignment between

sapphire and 2H-MoS_2 plays a role in the orientation of the MoS_2 nanoribbons on the (0001)-oriented sapphire substrate. In Fig. 5, we describe the growth mechanism of the MoS_2 nanoribbons. A uniform MoO_x film is covered with 20 nm NaF to serve as a precursor (Fig. 5a). The high-temperature reaction between the NaF and MoO_x, primarily consisting of MoO_3, see XPS data in Fig. S1, creates the Na-Mo-O liquid phase (Fig. 5b), following the possible chemical reaction route [38]:

$$3MoO_3(s) + 2NaF(s) \xrightarrow{highT} Na_2Mo_2O_7(l) + MoO_2F_2(g) \quad (2)$$

When exposed to sulfur vapours at high temperatures, MoS_2 solid crystals precipitate at some point defect within the liquid droplets, which can act as crystallisation centres for growth [42,46–49]. At high temperatures, the MoS_2 crystals in a liquid phase can diffuse and merge into larger multilayer MoS_2 domains (Fig. 5d). The MoS_2 crystals are then formed following the second possible reaction, as described below:

$$Na_2Mo_2O_7(l) + S(g) \xrightarrow{900^oC} MoS_2(s) + Na_2SO_4(g) \longrightarrow MoS_2(s) + Na_2S(s) + SO_3(g)\uparrow$$

We assume that crystals observed in Fig. S12 and S13 may be good candidates for the proposed process. The crystal expands horizontally following the most favourable surface energy, forming long multilayer MoS_2 nanoribbons. The nanoribbon length is likely limited by the droplet size and precursor amount (Fig. 5e). The nanoribbon can collide with other liquid droplets on the surface during the unidirectional growth (Fig. 5f). The MoS_2 crystals in a liquid phase surrounding the nanoribbon join the bottom layer. The latter guides the lateral expansion of the MoS_2 monolayer nanoribbon edges on both sides of the nanoribbon core (Fig. 3b,c). During cooling and solidification, the monolayer nanoribbon edge may remain attached to the nanoribbon core (Fig. 3b) or be detached from it due to a large intrinsic strain (Fig. S6). In stark contrast to previous reports, in which $Na_2Mo_2O_7$ particles remain at the terminal of the nanoribbons [42], our nanoribbons are free of reminiscence alkali salts. This is probably because the precursor is fully consumed during growth. In addition, small liquid droplets with a low precursor concentration, homogeneously distributed on sapphire, give rise to triangles MoS_2, which can be identified in Fig. 3 and Fig. S6, S11. The AFM images in Fig. S11 show a high fraction of single layer (1L) and occasionally bilayer MoS_2 crystals.

Raman spectroscopy. Single-point Raman spectra and Raman mapping of the as-grown nanoribbons and triangles MoS_2 are illustrated in Fig. 6. The Raman spectra were tailored using multi-Lorentzian peak fitting. The spectra contain first-order optical modes at the Brillouin zone centre, i.e., in-plane E^1_{2g} (Γ) and out-of-plane A_{1g}(Γ), and a zone-edge mode 2LA(*M*) activated by the disorder. The longitudinal acoustic phonons LA(M) are in-plane collective movements of the atoms in the lattice, while the symbol (M) refers to the M−point of the Brillouin zone. Two-phonon E^2_{1u}(Γ-A) and Raman sapphire peak (marked with *) are also observed. Fig. 6a shows a single-point Raman spectrum obtained from the core of the MoS_2 nanoribbon with E^1_{2g} (Γ) and A_{1g}(Γ) peak positions at 385 cm^{-1} and 409 cm^{-1}, respectively. This corresponds to a peak difference (Δk) of nearly 26 cm^{-1}, characteristic for bulk MoS_2, with a low full width at half maximum (FWHM) of the E^1_{2g} (Γ) and A_{1g}(Γ) peaks of 3.8 cm^{-1} and 3.1 cm^{-1}, respectively. The narrow Raman peaks with high intensity may suggest that the MoS_2 nanoribbon is a single crystal.

Interestingly, the Raman spectra change significantly for the triangularly shaped MoS_2 crystals (see Fig. 6b). Here, E^1_{2g}(Γ) and A_{1g}(Γ) Raman peaks exhibit strong broadening, and a pronounced contribution from the sapphire substrate is evident. The Raman peaks are positioned at 380 cm^{-1} and 407 cm^{-1} (Δk of nearly 27 cm^{-1}), with FWHM values of 7.0 cm^{-1} and 9.0 cm^{-1}, respectively. A considerable broadening of the Raman peaks and a high Δk value may be associated with small multilayer crystals, significant strain, and doping of the MoS_2 crystal. The high-resolution Raman intensity mapping shown in Fig. 6(c-f) reveals that the MoS_2 nanoribbons are surrounded by triangular crystals, similar to Fig. 3. The Raman maps reveal that the triangular crystals exhibit a significant Raman shift compared to the nanoribbons. Moreover, the intensity profile is uniform along the core of the nanoribbon, while the nanoribbon edges appear dimmer than the core. The lower intensities at the edges are attributed to the monolayer nanoribbons. Single-point Raman spectra acquired on the various arms of the tree-like ribbons highlighted in Fig. 5a did not reveal any significant difference (not shown).

Intrinsic strain in MoS_2 nanostructures. The AFM images in Fig. S11 reveal that triangular crystals are predominantly mono- and bilayers MoS_2, which does not match with the experimentally determined Δk values of nearly 27 cm^{-1} from the mono- and bilayer MoS_2. The specimens were transferred onto a sapphire substrate to understand the effect of strain on these distinct Raman features of MoS_2. The optical images of the transferred specimens containing ribbons and triangular MoS_2 crystals are shown in Fig. 7(a-c). Fig. 7(d-f) shows comparisons between the Raman spectra of the as-grown MoS_2 (black curves) and transferred MoS_2 onto a sapphire substrate (red curves). The Raman spectra of the as-grown and transferred 2D MoS_2 triangles are distinct in terms of peak intensity ratios, peak positions, and peak widths (the details are presented in Tables T1 and T2 in SI). The Raman spectrum

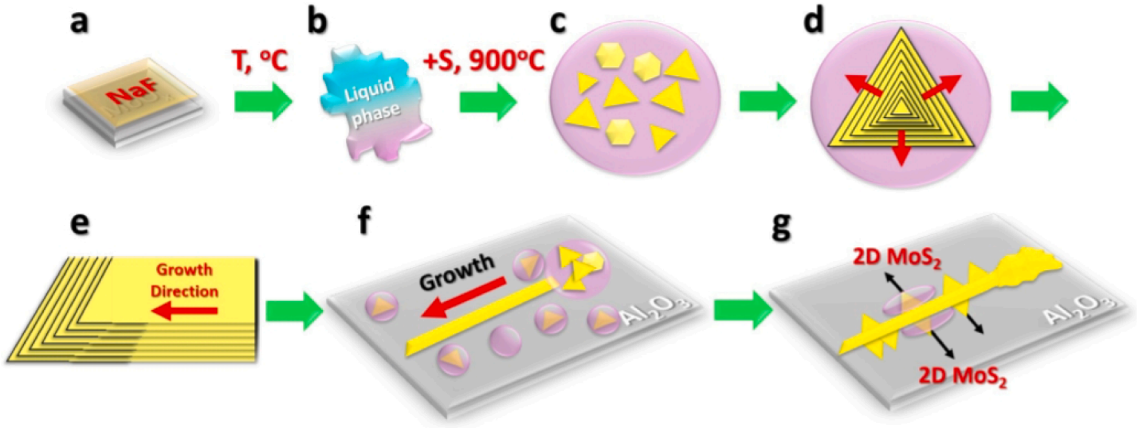

Fig. 5. The growth mechanism of MoS_2 nanoribbons. a) The precursor is a MoO_x thin film covered with a 20 nm NaF layer; b) A liquid phase forms at an elevated temperature upon the reaction between the MoO_x and NaF layers; c) MoS_2 nanoribbon seed crystals are formed in the liquid phase upon exposure to sulfur vapour; d) The MoS_2 multilayer domains form in the liquid phase; e) The MoS_2 nanoribbon grows unidirectional from a seed crystal; f) The MoS_2 nanoribbon surrounded by liquid phase islands expands on the surface from an initial droplet; g) Lastly, the 2D MoS_2 layers surrounding the nanoribbon form triangular crystals on the surface, while the initial liquid droplet solidifies.

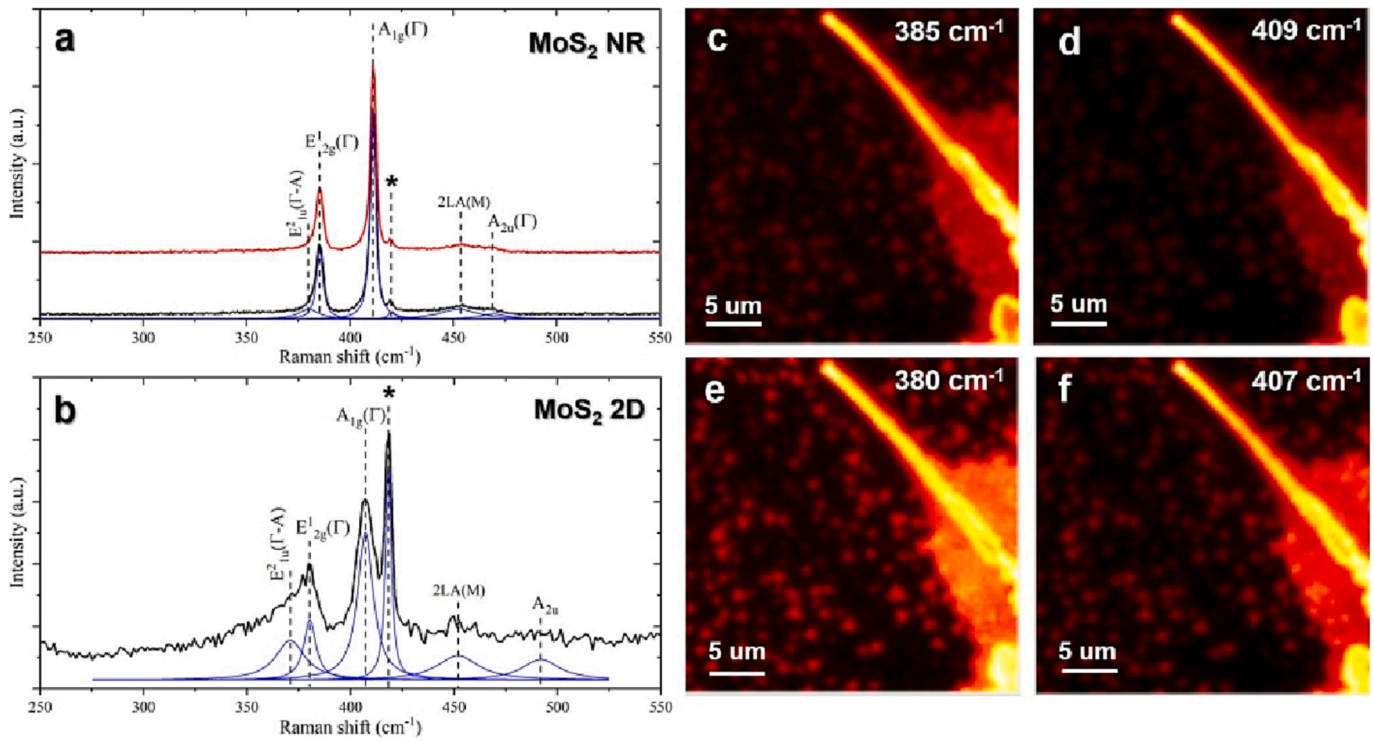

Fig. 6. Raman spectra of the MoS_2 nanoribbon (NR) and triangle (2D). a) Single-point Raman spectrum obtained from the MoS_2 nanoribbon (red, black) and its deconvolution (blue); b) single-point Raman spectrum obtained from the MoS_2 triangle (black) and its deconvolution (blue). Raman mapping of the peak intensities of the MoS_2 nanoribbons located at (c) 385.0 cm^{-1} and (d) 409.0 cm^{-1}, and MoS_2 triangles located at (e) 380.0 cm^{-1} and (f) 407.0 cm^{-1}.

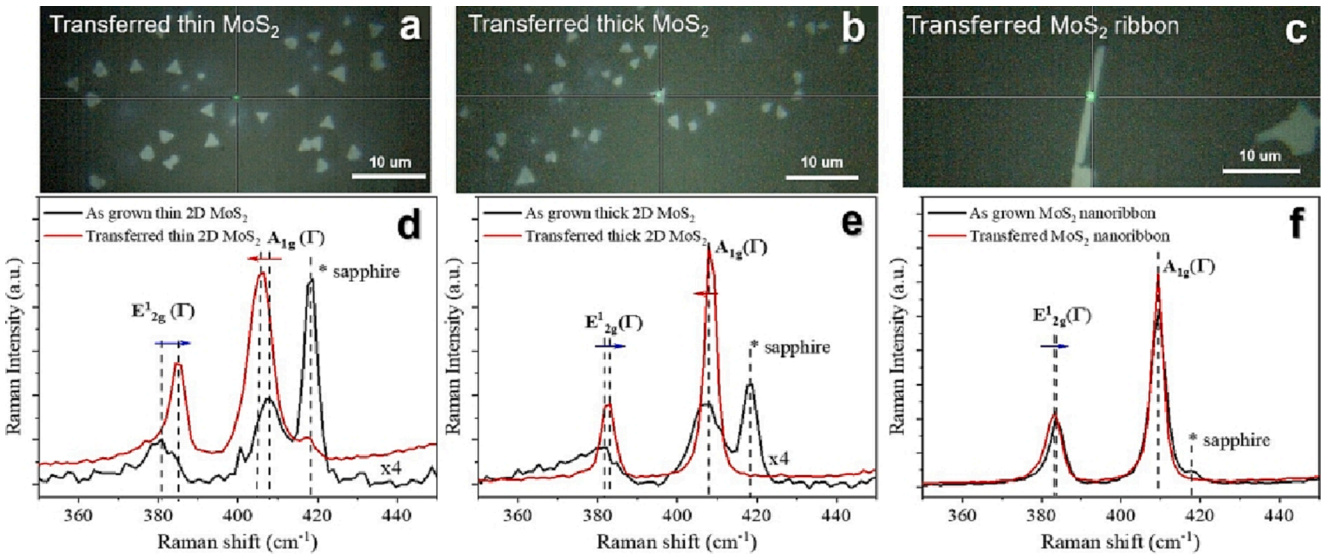

Fig. 7. Optical images and Raman spectra of the strained (as-grown) and unstrained (transferred) MoS_2. (a-c) Optical images of the transferred MoS_2 triangles and nanoribbons. The cross mark with a small dot in the middle indicates the position of the laser beam. (d-f) Raman spectra of various MoS_2 crystals before and after the transfer, namely 2D-MoS_2 (d), thick multilayer triangular MoS_2 (e), and MoS_2 nanoribbons (f). Black and red curves show the spectra of the as-grown and transferred samples. Blue and red arrows indicate the blue and red Raman shifts, respectively.

shown in Fig. 7d reveals a blueshift of the E^1_{2g} mode of 4.5 cm^{-1} and a redshift of the A_{1g} mode of 1.8 cm^{-1} between the transferred and the as-grown 2D MoS_2. This corresponds to a Δk value of 20.7 cm^{-1} for the transferred specimen characteristic of a CVD-grown monolayer MoS_2. A similar trend was observed for the other transferred specimens. However, we note that the shift of the A_{1g} and E^1_{2g} Raman modes in multilayer triangles and nanoribbons MoS_2 is much less pronounced than for the monolayer counterparts (Fig. 7e,f). Figs. S12 and S13 show multilayer triangular crystals of MoS_2 and some additional Raman spectra obtained from distinct regions with nanoribbons and monolayers (Figs. S14, S15).

The softening of the E^1_{2g} and hardening of the A_{1g} Raman modes, as well as the broadening of the Raman peaks, are a clear indication of the presence of strain in the as-grown MoS_2 monolayers [50–52]. A similar shift in the in-plane E^1_{2g} Raman mode of MoS_2 was observed by McCreary et al.[53], i.e., 5.2 cm^{-1} as compared to our work of 3.5 cm^{-1}. Under a strain of 1.49 %, Li et al. reported a redshift of the E^1_{2g} peak of 11.1 cm^{-1}

with an average slope of about 7.4 cm^{-1}% strain [54], which is also much larger than our data. Upon transfer, the strain within the monolayers is effectively released, and Raman spectra closely match those of the CVD monolayers [46,55]. Lastly, the A_{1g} mode related to the out-of-plane vibrations of the sulfur atoms in the lattice is less sensitive to strain than the in-plane E^1_{2g} Raman mode. The shift of the A_{1g} can be attributed to residual doping due to the presence of Na-containing residues on the surface [56] (Fig. S3).

We note that the strain measured in the 2D MoS_2 triangles is biaxial and not uniaxial, as we do not observe a measurable splitting of the E^0 mode as the strain breaks the symmetry of the crystal [57,54]. In this work, the specimens were cooled from the growth temperature of 900 °C at a rate of 20 °C/min. This natural cooling rate is sufficient to induce built-in strain in MoS_2 due to the mismatch between the thermal expansion coefficient (TEC) of sapphire and MoS_2 [58]. Indeed, sapphire has a TCE of $5.5 \times 10^{-6}K^{-1}$, which is 10 times larger than MoS_2 of $0.5 \times 10^{-6}K^{-1}$ [59]. We must note, however, that the reported TECs of MoS_2 vary broadly in the literature. Lin et al. estimated a TCE of $0.5 \times 10^{-6}K^{-1}$ [59], Su et al. reported an in-plane TEC of MoS_2 is $2.48 \times 10^{-6}K^{-1}$ at room temperature [60], whereas Lu et al. reported a TEC of $8.2 \times 10^{-6}K^{-1}$ [61]. These discrepancies arise from the difference in the biaxial strain coefficient of the Raman mode employed in the calculations and whether the effect of the substrate is considered.

The Raman spectra of the multilayer triangular and nanoribbon crystals are also affected by strain. The strain is linearly dependent on the thickness of the layered material. Hence, the smaller strain observed in the thick triangles of MoS_2 could be understood as the variation of local strain with increasing crystal thickness [62]. In the case of the nanoribbons, the mechanical strain may be more effective along the expansion direction of the nanoribbons. We hypothesise that the built-in strain in nanoribbons is released via fracturing, as indicated in the AFM images in Fig. 4. The abnormal behaviour of nanoribbons is not fully understood, nor is the role of defects in the thermal stability of the nanoribbons at elevated temperatures. Future studies must be conducted to shed light on the interplay between nanoribbon dimensions and their dependence on the thermal expansion coefficient.

4. Conclusion

In summary, we have demonstrated the growth of oriented multilayer MoS_2 nanoribbons using a NaF-assisted process via the sulfurisation of PLD-grown MoO_x solid oxide precursors in a sulfur-rich environment. The process results in the formation of multilayer MoS_2 nanoribbons, together with a large amount of mono- and multilayer MoS_2 triangular crystals. The as-synthesized nanoribbons exhibit a typical width of up to 800 nm and length of 10–20 μm, resulting in a width-to-length ratio of nearly 30. The nanoribbons feature a tree-like structure with three-, four-, and multi-directions with a V-shape of 60° and 120° or a Y-shape with 120°. Raman spectroscopy mapping reveals a considerable biaxial strain in the as-grown specimens. The highest strain is observed in the as-grown 2D MoS_2 crystals and is effectively released upon transfer. Lastly, in the case of the MoS_2 nanoribbons, the built-in strain is likely released via the rupture of the nanostructures. Our work depicts a step toward understanding the different growth modes observed in the metal-halide-assisted CVD process for TMD synthesis.

CRediT authorship contribution statement

Denys I. Miakota: Conceptualization, Investigation, Formal analysis, Writing – original draft. **Ganesh Ghimire:** Conceptualization, Investigation, Formal analysis. **Rajesh Kumar Ulaganathan:** Investigation. **Moises E. Rodriguez:** Investigation. **Stela Canulescu:** Investigation, Formal analysis, Writing – review & editing, Supervision, Funding acquisition.

Declaration of Competing Interest

The authors declare that they have no known competing financial interests or personal relationships that could have appeared to influence the work reported in this paper.

Data availability

No data was used for the research described in the article.

Acknowledgements

Stela Canulescu acknowledges the support from the Independent Research Fund Denmark, Sapere Aude grant (project number 8049-00095B).

Declarations

The authors declare no competing financial interest.

References

[1] G. Bae, et.al., 3 nm GAA technology featuring multi-bridge-channel FET for low power and high performance applications (2018). Doi: 10.1109/IEDM.2018.8614629.
[2] M. Tilli, T. Motooka, V.-M. Airaksinen, S. Franssila, M. Paulasto-Kröckel, V. Lindroos, Handbook of Silicon Based MEMS Materials and Technologies. Elsevier Inc., Amsterdam, 2020.
[3] R. Xu, Y. Xu, Modern Inorganic Synthetic Chemistry, Elsevier B.V, Amsterdam, 2017.
[4] M. Uwaha, Growth kinetics: Basics of crystal growth mechanisms. In: T. Nishinaga (ed.) Handbook of Crystal Growth (Second Edition), Second edition edn., pp. 359–399. Elsevier, Boston (2015). Doi: 10.1016/B978-0-444-56369-9.00008-3.
[5] Y. Kang, et.al., $Ge_{0.95}Sn_{0.05}$ gate-all-around p-channel metal-oxidesemiconductor field-effect transistor with sub-3 nm nanowire width, Nano Lett. **21**(13) (2021) 5555–5563.
[6] L. Dong, A. Subramanian, B.J. Nelson, Carbon nanotubes for nanorobotics, Nano Today 2 (6) (2007) 12–21, https://doi.org/10.1016/S1748-0132(07)70169-X.
[7] V.N. Popov, Carbon nanotubes: properties and application, Mater. Sci. Eng.: Rep. 43 (3) (2004) 61–102, https://doi.org/10.1016/j.mser.2003.10.001.
[8] A.K. Geim, K.S. Novoselov, The rise of graphene, Nat. Mater. 6 (3) (2013) 18, https://doi.org/10.1038/nmat1849.
[9] H. Yufeng, et al., The role of surface oxygen in the growth of large singlecrystal graphene on copper, Science 342 (6159) (2013) 720–723, https://doi.org/10.1126/science.1243879.
[10] X. Chen, L. Zhang, S. Chen, Large area CVD growth of graphene, Synthet. Met. 210 (2015) 95–108, https://doi.org/10.1016/j.synthmet. 2015.07.005.
[11] H.C.P. Movva, et al., High-mobility holes in dual-gated wse_2 field-effect transistors, ACS Nano 9 (10) (2015) 10402–10410, https://doi.org/10.1021/acsnano.5b04611.

A novel two-step route to unidirectional growth of multilayer MoS2

[12] H.-W. Guo, Z. Hu, Z.-B. Liu, J.-G. Tian, Stacking of 2D materials, Adv. Funct. Mater. 31 (4) (2021) 2007810, https://doi.org/10.1002/adfm.202007810.
[13] D. Jariwala, D.V.K. Sangwan, L.J. Lauhon, T.J. Marks, M.C. Hersam, Emerging device applications for semiconducting two-dimensional transition metal dichalcogenides, ACS Nano 8 (2) (2014) 1102–1120, https://doi.org/10.1021/nn500064s.
[14] Z. Chen, A. Narita, K. Müllen, Graphene nanoribbons: on-surface synthesis and integration into electronic devices. Adv. Mater. 32(45) (2020) 2001893 (2020). Doi: 10.1002/adma.202001893.
[15] Y. Gu, Z. Qiu, K. Müllen, Nanographenes and graphene nanoribbons as multitalents of present and future materials science, J. Am. Chem. Soc. 144(26) (2022) 11499–11524. Doi: 10.1021/jacs.2c02491.
[16] Y. Huang, et al., Logic gates and computation from assembled nanowire building blocks, Science 294 (5545) (2001) 1313–1317, https://doi.org/10.1126/science.1066192.
[17] L. Liu, P. Song, Z. Yang, Q. Wang, Highly sensitive and selective trimethylamine sensors based on WO_3 nanorods decorated with au nanoparticles, Physica E 90 (2017) 109–115, https://doi.org/10.1016/j.physe.2017.03.025.
[18] T. Roy, M. Tosun, X. Cao, H. Fang, D.-H. Lien, P. Zhao, Y.Z. Chen, Y.-L. Chueh, J. Guo, A. Javey, Dual-gated MoS_2/WSe_2 van der waals tunnel diodes and transistors, ACS Nano 9 (2) (2015) 2071–2079, https://doi.org/10.1021/nn507278b.
[19] F.A. Rasmussen, K.S. Thygesen, Computational 2D materials database: electronic structure of transition-metal dichalcogenides and oxides, J. Phys. Chem. C 119 (23) (2015) 13169–13183, https://doi.org/10.1021/acs.jpcc.5b02950.

[20] C. Cong, J. Shang, X. Wu, B. Cao, N. Peimyoo, C. Qiu, L. Sun, T. Yu, Synthesis and optical properties of large-area single-crystalline 2D semiconductor WS_2 monolayer from chemical vapor deposition, Adv. Opt. Mater. 2 (2) (2014) 131–136, https://doi.org/10.1002/adom. 201300428.

[21] Y.-T. Ho, C.-H. Ma, T.-T. Luong, L.-L. Wei, T.-C. Yen, W.-T. Hsu, W.-H. Chang, Y.-C. Chu, Y.-Y. Tu, K.P. Pande, E.Y. Chang, Layered MoS_2 grown on c-sapphire by pulsed laser deposition, Physica Status Solidi-Rapid Res. Lett. 9 (3) (2015) 187–191, https://doi.org/10.1002/pssr.201409561.

[22] Y. Jeon, J. Seo, J. Kim, D. Rhee, M. Jung, H. Park, J. Kang, Wafer-scale two-dimensional molybdenum diselenide phototransistor array via liquid-precursor-assisted chemical vapor deposition, Adv. Opt. Mater. 10 (3) (2022) 2101492, https://doi.org/10.1002/adom. 202101492.

[23] K.R. Paton, E. Varrla, C. Backes, R.J. Smith, U. Khan, A. O'Neill, C. Boland, M. Lotya, O.M. Istrate, P. King, T. Higgins, S. Barwich, P. May, P. Puczkarski, I. Ahmed, M. Moebius, H. Pettersson, E. Long, J. Coelho, S.E. O'Brien, E. K. McGuire, B.M. Sanchez, G.S. Duesberg, N. McEvoy, T.J. Pennycook, C. Downing, A. Crossley, V. Nicolosi, J.N. Coleman, Scalable production of large quantities of defect-free few-layer graphene by shear exfoliation in liquids, Nat. Mater. 13 (6) (2014) 624–630, https://doi.org/10.1038/nmat3944.

[24] Q. Feng, N. Mao, J. Wu, H. Xu, C. Wang, J. Zhang, L. Xie, Growth of $MoS_{(1-x)}Se_x$ (x = 0.41–1.00) monolayer alloys with controlled morphology by physical vapor deposition, ACS Nano 9 (7) (2015) 7450–7455, https://doi.org/10.1021/acsnano.5b02506.

[25] C. Yim, N. McEvoy, S. Riazimehr, D.S. Schneider, F. Gity, S. Monaghan, P. K. Hurley, M.C. Lemme, G.S. Duesberg, Wide spectral photoresponse of layered platinum diselenide-based photodiodes, Nano Lett. 18 (3) (2018) 1794–1800, https://doi.org/10.1021/acs.nanolett.7b05000.

[26] R.I. Romanov, M.G. Kozodaev, D.I. Myakota, A.G. Chernikova, et al., Synthesis of large area two-dimensional MoS_2 films by sulfurization of atomic layer deposited MoO_3 thin film for nanoelectronic applications, ACS Nano 2 (12) (2019) 7521–7531, https://doi.org/10.1021/acsanm. 9b01539.

[27] M. Nakano, Y. Wang, Y. Kashiwabara, H. Matsuoka, Y. Iwasa, Layerby-layer epitaxial growth of scalable wse_2 on sapphire by molecular beam epitaxy, Nano Lett. 17 (9) (2017) 5595–5599, https://doi.org/10.1021/acs.nanolett.7b02420.

[28] J. Hall, B. Pielić, C. Murray, W. Jolie, T. Wekking, C. Busse, M. Kralj, T. Michely, Molecular beam epitaxy of quasi-freestanding transition metal disulphide monolayers on van der Waals substrates: A growth study, 2D Mater. 5 (2) (2018), https://doi.org/10.1088/2053-1583/aaa1c5.

[29] F. Bertoldo, R.R. Unocic, Y.-C. Lin, X. Sang, A.A. Puretzky, Y. Yu, D. Miakota, C. M. Rouleau, J. Schou, K.S. Thygesen, D.B. Geohegan, S. Canulescu, Intrinsic defects in MoS_2 grown by pulsed laser deposition: from monolayers to bilayers, ACS Nano 15 (2) (2021) 2858–2868, https://doi.org/10.1021/acsnano.0c08835.

[30] M.I. Serna, S.H. Yoo, S. Moreno, Y. Xi, J.P. Oviedo, H. Choi, H.N. Alshareef, M. J. Kim, M Minary-Jolandan, M.A. Quevedo-Lopez, Large-area deposition of MoS_2 by pulsed laser deposition with in situ thickness control, ACS Nano 10 (2016) 6054, https://doi.org/10.1021/acsnano.6b01636.

[31] G. Siegel, Y.P. Venkata Subbaiah, M.C. Prestgard, A. Tiwari, Growth of centimeter-scale atomically thin MoS_2 films by pulsed laser deposition, APL Mater. 3 (5) (2015) 56103, https://doi.org/10.1063/1.4921580.

[32] X. Xu, Z. Wang, S. Lopatin, M.A. Quevedo-Lopez, H.N. Alshareef, Wafer scale quasi single crystalline MoS_2 realized by epitaxial phase conversion, 2D Mater. 6(1) (2019). Doi: 10.1088/2053-1583/ aaf3e9.

[33] X. Xu, G. Das, X. He, M.N. Hedhili, E.D. Fabrizio, X. Zhang, H.N. Alshareef, High-performance monolayer MoS_2 films at the wafer scale by two-step growth, Adv. Funct. Mater. 29 (32) (2019) 1901070, https://doi.org/10.1002/adfm.201901070.

[34] D.I. Miakota, R.R. Unocic, F. Bertoldo, G. Ghimire, S. Engberg, D. Geohegan, K. S. Thygesen, S. Canulescu, A facile strategy for the growth of high-quality tungsten disulfide crystals mediated by oxygendeficient oxide precursors, Nanoscale 14 (26) (2022) 9485–9497, https://doi.org/10.1039/d2nr01863b.

[35] M.G. Kozodaev, A.S. Slavich, R.I. Romanov, S.S. Zarubin, A.M. Markeev, Influence of reducing agent on properties of thin WS_2 nanosheets prepared by sulfurization of atomic layer-deposited WO_3, J. Phys. Chem. C 124 (51) (2020) 28169–28177, https://doi.org/10.1021/acs.jpcc.0c09769.

[36] R.I. Romanov, M.G. Kozodaev, A.G. Chernikova, I.V. Zabrosaev, A.A. Chouprik, S. S. Zarubin, S.M. Novikov, V.S. Volkov, A.M. Markeev, Thickness-dependent structural and electrical properties of WS_2 nanosheets obtained via the ALD-grown WO_3 sulfurization technique as a channel material for field-effect transistors, ACS Omega 6 (50) (2021) 34429–34437, https://doi.org/10.1021/acsomega.1c04532.

[37] M. Mattinen, M. Leskelà, M. Ritala, Atomic layer deposition of 2D metal dichalcogenides for electronics, catalysis, energy storage, and beyond, Adv. Mater. Interfaces 8(6) (2021). Doi: 10.

[38] S. Li, et al., Vapour–liquid–solid growth of monolayer MoS_2 nanoribbons, Nat. Mater. 17 (6) (2018) 535–542, https://doi.org/10.1002/adfm. 202007810.

[39] S.C. Dhanabalan, J.S. Ponraj, H. Zhang, Q. Bao, Present perspectives of broadband photodetectors based on nanobelts, nanoribbons, nanosheets and the emerging 2D materials, Nanoscale 8 (12) (2016) 6410–6434, https://doi.org/10.1039/c5nr09111j.

[40] A.R. Botello-Mendez, F. Lopez-Urias, M. Terrones, H. Terrones, Metallic and ferromagnetic edges in molybdenum disulfide nanoribbons, Nanotechnology 20 (32) (2009), https://doi.org/10.1088/0957-4484/20/32/325703.

[41] T. Hu, J. Zhou, J. Dong, Y. Kawazoe, Electronic and magnetic properties of armchair MoS_2 nanoribbons under both external strain and electric field, studied by first principles calculations, J. Appl. Phys. 116 (6) (2014), https://doi.org/10.1063/1.4891997.

[42] D. Wu, J. Shi, X. Zheng, J. Liu, W. Dou, Y. Gao, X. Yuan, F. Ouyang, H. Huang, Cvd grown MoS_2 nanoribbons on MoS_2 covered sapphire(0001) without catalysts, Physica Status Solidi (RRL) – Rapid Research Letters 13 (7) (2019) 1900063https://onlinelibrary.wiley.com/doi/pdf/10.1002/pssr.201900063, https://doi.org/10.1002/pssr.201900063.

[43] T. Chowdhury, J. Kim, E.C. Sadler, C. Li, S.W. Lee, K. Jo, W. Xu, D.H. Gracias, N. V. Drichko, D. Jariwala, T.H. Brintlinger, T. Mueller, H.-G. Park, T.J. Kempa, Substrate-directed synthesis of MoS_2 nanocrystals with tunable dimensionality and optical properties, Nat. Nanotechnol. 15 (1) (2020) 29, https://doi.org/10.1038/s41565-019-0571-2.

[44] Z. Li, Z. Jiang, W. Zhou, M. Chen, M. Su, X. Luo, T. Yu, C. Yuan, MoS_2 nanoribbons with a prolonged photoresponse lifetime for enhanced visible light photoelectrocatalytic hydrogen evolution, Inorg. Chem. 60 (3) (2021) 1991–1997, https://doi.org/10.1021/acs.inorgchem. 0c03478.

[45] A.I. Dago, Y.K. Ryu, F.J. Palomares, R. Garcia, Direct patterning of p-type-doped few-layer wse_2 nanoelectronic devices by oxidation scanning probe lithography, ACS Appl. Mater. Interfaces 10 (46) (2018) 40054–40061, https://doi.org/10.1021/acsami.8b15937.

[46] D. Dumcenco, D. Ovchinnikov, K. Marinov, P. Lazić, M. Gibertini, N. Marzari, O. L. Sanchez, Y.-C. Kung, D. Krasnozhon, M.-W. Chen, S. Bertolazzi, P. Gillet, A. i Morral, A. Radenovic, A. Kis, Large-area epitaxial monolayer MoS_2, ACS Nano 9 (2015) 4611–4620, https://doi.org/10.1021/acsnano.5b01281.

[47] X. Qiang, Y. Iwamoto, A. Watanabe, et al., Non-classical nucleation in vapor–liquid–solid growth of monolayer WS_2 revealed by in-situ monitoring chemical vapor deposition, Sci. Rep. 11 (22285) (2021), https://doi.org/10.1038/s41598-021-01666-9.

[48] L. Zhang, H. Nan, X. Zhang, et al., 2d atomic crystal molecular superlattices by soft plasma intercalation, Nat. Commun. 11 (5960) (2020), https://doi.org/10.1038/s41467-020-19766-x.

[49] X. Zhang, L. Huangfu, Z. Gu, S. Xiao, J. Zhou, H. Nan, X. Gu, K.K. Ostrikov, Controllable epitaxial growth of large-area MoS_2/WS_2 vertical heterostructures by confined-space chemical vapor deposition, Small 17 (18) (2021) 2007312, https://doi.org/10.1002/smll.202007312.

[50] A. Castellanos-Gomez, R. Roldán, E. Cappelluti, M. Buscema, F. Guinea, H.S.J. van der Zant, G.A. Steele, Local strain engineering in atomically thin MoS_2. Nano Lett. 13(11) (2013) 5361–5366 (2013). Doi: 10.1021/nl402875m.

[51] J.O. Island, A. Kuc, E.H. Diependaal, R. Bratschitsch, H.S.J. van der Zant, T. Heine, A. Castellanos-Gomez, Precise and reversible band gap tuning in single-layer $MoSe_2$ by uniaxial strain, Nanoscale 8 (2016) 2589–2593, https://doi.org/10.1039/C5NR08219F.

[52] K. He, C. Poole, K.F. Mak, J. Shan, Experimental demonstration of continuous electronic structure tuning via strain in atomically thin MoS_2.

[53] A. McCreary, R. Ghosh, M. Amani, J. Wang, K.-A.-N. Duerloo, A. Sharma, K. Jarvis, E.J. Reed, A.M. Dongare, S.K. Banerjee, M. Terrones, R.R. Namburu, M. Dubey, Effects of uniaxial and biaxial strain on few-layered terrace structures of MoS_2 grown by vapor transport, ACS Nano 10 (3) (2016) 3186–3197, https://doi.org/10.1021/acsnano.5b04550. PMID: 26881920.

[54] Z. Li, Y. Lv, L. Ren, J. Li, L. Kong, Y. Zeng, Q. Tao, R. Wu, H. Ma, B. Zhao, D. Wang, W. Dang, K. Chen, L. Liao, X. Duan, X. Duan, Y. Liu, Efficient strain modulation of 2d materials via polymer encapsulation, Nat. Commun. 11 (1) (2020), https://doi.org/10.1038/s41467-020-15023-3.

[55] L. Zhang, H. Nan, S. Xiao, et al., Transition metal dichalcogenides bilayer single crystals by reverse-flow chemical vapor epitaxy, Nat. Commun. 10 (598) (2019), https://doi.org/10.1038/s41467-019-08468-8.

[56] Z. Cui, X. Wang, Y. Ding, C. Zhang, M. Li, Alkali-metal-embedded in monolayer MoS_2: optical properties and work functions, Opt. Quant. Electron. 50 (9) (2018), https://doi.org/10.1007/s11082-018-1612-z.

[57] H.J. Conley, B. Wang, J.I. Ziegler, R.F. Haglund Jr., S.T. Pantelides, K.I. Bolotin, Bandgap engineering of strained monolayer and bilayer MoS_2, Nano Lett. 13 (8) (2013) 3626–3630, https://doi.org/10.1021/nl4014748.

[58] G.H. Ahn, M. Amani, H. Rasool, D.-H. Lien, J.P. Mastandrea, J.W. Ager III, M. Dubey, D.C. Chrzan, A.M. Minor, A. Javey, Strainengineered growth of two-dimensional materials, Nat. Commun. 8 (2017), https://doi.org/10.1038/s41467-017-00516-5.

[59] Z. Lin, W. Liu, S. Tian, K. Zhu, Y. Huang, Y. Yang, Thermal expansion coefficient of few-layer MoS_2 studied by temperature-dependent raman spectroscopy, Sci. Rep. 11 (1) (2021), https://doi.org/10.1038/s41598-021-86479-6.

[60] L. Su, Y. Zhang, Y. Yu, L. Cao, Dependence of coupling of quasi 2-d MoS_2 with substrates on substrate types, probed by temperature dependent raman scattering, Nanoscale 6 (9) (2014) 4920–4927, https://doi.org/10.1039/c3nr06462j.

[61] X. Lu, X. Luo, J. Zhang, S.Y. Quek, Q. Xiong, Lattice vibrations and raman scattering in two-dimensional layered materials beyond graphene, Nano Res. 9 (12) (2016) 3559–3597, https://doi.org/10.1007/s12274-016-1224-5.

[62] H.J. Conley, et al., Bandgap engineering of strained monolayer and bilayer MoS_2, Nano Lett. 13 (8) (2013) 3626–3630, https://doi.org/10.1021/nl4014748.